

# Certain properties of MUSIC-type imaging functional in inverse scattering from an open, sound-hard arc

Won-Kwang Park

*Department of Mathematics, Kookmin University, Seoul, 136-702, Korea.*

---

## Abstract

This paper concerns mathematical formulation of well-known Multiple Signal Classification (MUSIC)-type imaging functional in the inverse scattering problem by an open sound-hard arc. Based on the physical factorization of so-called Multi-Static Response (MSR) matrix and the structure of left-singular vectors linked to the non-zero singular values of MSR matrix, we construct a relationship between imaging functional and Bessel function of order 1 of the first kind. We then expound certain properties of MUSIC and present numerical results for a number of differently chosen smooth arcs.

*Key words:* Multiple Signal Classification (MUSIC), sound-hard arc, Multi-Static Response (MSR) matrix, Bessel function, numerical results

---

## 1. Introduction

The main purpose of this paper is to identify mathematical structure of so-called Multiple Signal Classification (MUSIC)-type imaging functional for two-dimensional perfectly conducting, arc-like smooth cracks at a fixed frequency. From our best knowledge, the mathematical modeling of time-harmonic inverse scattering problem from a sound-hard open arc has been considered in [1]. In this remarkable paper, a boundary integral equation approach has been concerned for solving the direct scattering problem a complete description of a numerical solution method including a rigorous convergence and error analysis is considered. Then, the inverse scattering problem related to retrieval of the sound-hard crack based on Newton-type iterative scheme has been investigated in [2]. After the successful application, in many works [3, 4, 5, 6], many authors have proposed various algorithms, most of which are based on Newton-type iteration schemes.

Generally, for a successful application of Newton-type iterative based scheme, a good initial guess that is close to the unknown crack must be applied in the beginning of iteration procedure in order to avoid the non-convergence phenomenon. For this reason, various non-iterative shape reconstruction algorithms. Specifically, Multiple Signal Classification

---

*Email address:* parkwk@kookmin.ac.kr (Won-Kwang Park)

(MUSIC) has been shown to be feasible in various inverse scattering problems and generalized to the shape reconstruction of various kind of targets in two- and three-dimensional problems. Related works can be found in [7, 8, 9, 10, 11, 12, 13, 14, 15, 16, 17] and references therein. In recent works [18, 19], the structure of MUSIC was identified in full- and limited-view inverse scattering problem for imaging of sound-soft arc (Dirichlet boundary condition – Transverse Magnetic polarization) but as to the sound-soft arc, little has been theoretically studied.

Motivated by the above, this paper concerns the identification of some properties of the MUSIC-type imaging algorithm in full-view inverse scattering from sound-soft arcs at a fixed single frequency. For this purpose, we investigate a relationship between the MUSIC-type imaging function and the Bessel function of order 1 of the first kind in order to identify various properties of MUSIC.

This paper is constructed as follows. In section 2, we briefly survey the two-dimensional direct scattering problem from sound-soft arc and introduce MUSIC-type imaging algorithm. In section 3, we identify the structure of the MUSIC-type imaging function, and discover its certain properties. Some numerical experiments are shown in section 4 in order to support discovered properties. In section 5, a short conclusion is presented.

## 2. Direct scattering problem and MUSIC algorithm

### 2.1. Two-dimensional direct scattering problem from sound-hard arc

We briefly introduce the two-dimensional direct scattering problem by a perfectly conducting crack, denoted by  $\Gamma$ . We recommend [2] for a detailed discussion. Suppose that  $\Gamma$  is an oriented piecewise-smooth non-intersecting arc without a cusp that can be represented as

$$\Gamma := \{\gamma(s) : -1 \leq s \leq 1\}, \quad (1)$$

where  $\gamma \in \mathcal{C}^\infty$  is injective.

Let  $u(\mathbf{x}; \boldsymbol{\theta}) \in \mathcal{C}^2(\mathbb{R}^2 \setminus \Gamma) \cap \mathcal{C}(\overline{\mathbb{R}^2 \setminus \Gamma})$ , which is continuous at  $\gamma(-1)$  and  $\gamma(1)$ , be the total field that satisfying the following Helmholtz equation

$$\Delta u(\mathbf{x}; \boldsymbol{\theta}) + k^2 u(\mathbf{x}; \boldsymbol{\theta}) = 0 \quad \text{in } \mathbb{R}^2 \setminus \Gamma \quad (2)$$

with following Neumann boundary condition

$$\frac{\partial u(\mathbf{x}; \boldsymbol{\theta})}{\partial \mathbf{n}(\mathbf{x})} = 0 \quad \text{on } \Gamma \setminus \{\gamma(-1), \gamma(1)\}, \quad (3)$$

where  $\mathbf{n}(\mathbf{x})$  is a unit normal to  $\Gamma$  at  $\mathbf{x}$ .

It is well-known that  $u(\mathbf{x}; \boldsymbol{\theta})$  can be decomposed as  $u(\mathbf{x}; \boldsymbol{\theta}) = u_i(\mathbf{x}; \boldsymbol{\theta}) + u_s(\mathbf{x}; \boldsymbol{\theta})$ , where  $u_i(\mathbf{x}; \boldsymbol{\theta}) := e^{ik\boldsymbol{\theta} \cdot \mathbf{x}}$  be the given plane-wave incident field with direction  $\boldsymbol{\theta} \in \mathbb{S}^1$  and strictly positive wave number  $k$  and  $u_s(\mathbf{x}; \boldsymbol{\theta})$  be the unknown scattered field, which is demanded to satisfy the Sommerfeld radiation condition

$$\lim_{|\mathbf{x}| \rightarrow \infty} \sqrt{|\mathbf{x}|} \left( \frac{\partial u_s(\mathbf{x}; \boldsymbol{\theta})}{\partial |\mathbf{x}|} - iku_s(\mathbf{x}; \boldsymbol{\theta}) \right) = 0$$

uniformly into all directions  $\hat{\mathbf{x}} = \frac{\mathbf{x}}{|\mathbf{x}|}$ . Note that based on [2], we do not require any edge condition for the behavior of  $u(\mathbf{x}; \boldsymbol{\theta})$  at  $\gamma(-1)$  and  $\gamma(1)$ .

On the basis of result in [2],  $u_s(\mathbf{x}; \boldsymbol{\theta})$  can be expressed as the following double-layer potential

$$u_s(\mathbf{x}; \boldsymbol{\theta}) = \int_{\Gamma} \frac{\partial \Phi(\mathbf{x}, \mathbf{y})}{\partial \boldsymbol{\nu}(\mathbf{y})} \psi(\mathbf{y}, \boldsymbol{\theta}) d\mathbf{y} \quad \text{for } \mathbf{x} \in \mathbb{R}^2 \setminus \Gamma, \quad (4)$$

where  $-\psi(\mathbf{x}, \boldsymbol{\theta}) = u_+(\mathbf{x}, \boldsymbol{\theta}; k) - u_-(\mathbf{x}, \boldsymbol{\theta}; k)$ ,  $\Phi(\mathbf{x}, \mathbf{y})$  is the two-dimensional fundamental solution to the Helmholtz equation

$$\Phi(\mathbf{x}, \mathbf{y}) := \frac{i}{4} H_0^1(k |\mathbf{x} - \mathbf{y}|) \quad \text{for } \mathbf{x} \neq \mathbf{y},$$

and  $H_0^1$  denotes the Hankel function of order zero and of the first kind.

Suppose that for all  $\mathbf{x} \in \Gamma \setminus \{\gamma(-1), \gamma(1)\}$ , the limit of the following quantity exists:

$$\frac{\partial u_{\pm}(\mathbf{x}, \boldsymbol{\theta})}{\partial \mathbf{n}(\mathbf{x})} = \lim_{h \rightarrow +0} \nabla u(\mathbf{x} \pm h \mathbf{n}(\mathbf{x}), \boldsymbol{\theta}) \cdot \mathbf{n}(\mathbf{x}).$$

The far-field pattern  $u_{\infty}(\hat{\mathbf{x}}, \boldsymbol{\theta}; k)$  of the scattered field  $u_{\text{scat}}(\mathbf{x}, \boldsymbol{\theta}; k)$  is defined on the two-dimensional unit circle  $\mathbb{S}^1$ . It can be represented as

$$u_s(\mathbf{x}, \boldsymbol{\theta}) = \frac{e^{ik|\mathbf{x}|}}{\sqrt{|\mathbf{x}|}} \left\{ u_{\infty}(\hat{\mathbf{x}}, \boldsymbol{\theta}; k) + O\left(\frac{1}{|\mathbf{x}|}\right) \right\}$$

uniformly in all directions  $\hat{\mathbf{x}} = \mathbf{x}/|\mathbf{x}|$  and  $|\mathbf{x}| \rightarrow \infty$ . From the above representation and the asymptotic formula for the Hankel function, the far-field pattern can be written as

$$\begin{aligned} u_{\infty}(\hat{\mathbf{x}}, \boldsymbol{\theta}; k) &= -\frac{e^{i\frac{\pi}{4}}}{\sqrt{8\pi k}} \int_{\Gamma} \frac{\partial e^{-ik\hat{\mathbf{x}} \cdot \mathbf{y}}}{\partial \mathbf{n}(\mathbf{y})} \left( u_+(\mathbf{y}, \boldsymbol{\theta}; k) - u_-(\mathbf{y}, \boldsymbol{\theta}; k) \right) d\mathbf{y} \\ &= -\sqrt{\frac{k}{8\pi}} e^{-i\frac{\pi}{4}} \int_{\Gamma} \hat{\mathbf{x}} \cdot \mathbf{n}(\mathbf{y}) e^{-ik\hat{\mathbf{x}} \cdot \mathbf{y}} \psi(\mathbf{y}, \boldsymbol{\theta}; k) d\mathbf{y}. \end{aligned} \quad (5)$$

## 2.2. Introduction to MUSIC-type imaging

We apply the far-field pattern formula (5) to introduce MUSIC-type imaging functional. Before starting, we assume that the crack is divided into  $M$  different segments of size of the order of half the wavelength  $\lambda/2$ . With respect to the Rayleigh resolution limit, any detail less than one-half of the wavelength cannot be probed, and only one point, say  $\mathbf{y}_m$  for  $m = 1, 2, \dots, M$ , at each segment is expected to contribute at the image space of the response matrix  $\mathbb{K}(k)$  [20, 10, 14, 15]. Now, let us consider the eigenvalue structure of the MSR matrix, whose element is the collected far-field at observation number  $j$  for the incident number  $l$ :

$$\mathbb{K} := \left[ K_{jl}(\hat{\mathbf{x}}_j, \boldsymbol{\theta}_l; k) \right]_{j,l=1}^N = \left[ u_{\infty}(\hat{\mathbf{x}}_j, \boldsymbol{\theta}_l) \right]_{j,l=1}^N.$$

In this paper we assume that  $\hat{\mathbf{x}}_j = -\boldsymbol{\theta}_j$  for  $j = 1, 2, \dots, N$ , i.e., under the coincide configuration of incident and observation directions, the MSR matrix  $\mathbb{K}$  is complex symmetric. Therefore,  $\mathbb{K}$  can be decomposed as

$$\mathbb{K} = \sqrt{\frac{k}{8\pi}} e^{-i\frac{\pi}{4}} \int_{\Gamma} \mathbb{P}_N(\hat{\mathbf{x}}, \mathbf{y}) \mathbb{Q}_N(\hat{\mathbf{x}}, \mathbf{y})^T d\mathbf{y}, \quad (6)$$

where  $\mathbb{P}_N(\hat{\mathbf{x}}, \mathbf{y})$  is the illumination vector

$$\begin{aligned} \mathbb{P}_N(\hat{\mathbf{x}}, \mathbf{y}) &= - \left[ \hat{\mathbf{x}}_1 \cdot \mathbf{n}(\mathbf{y}) e^{-ik\hat{\mathbf{x}}_1 \cdot \mathbf{y}}, \hat{\mathbf{x}}_2 \cdot \mathbf{n}(\mathbf{y}) e^{-ik\hat{\mathbf{x}}_2 \cdot \mathbf{y}}, \dots, \hat{\mathbf{x}}_N \cdot \mathbf{n}(\mathbf{y}) e^{-ik\hat{\mathbf{x}}_N \cdot \mathbf{y}} \right]^T \Big|_{\hat{\mathbf{x}}_j = -\boldsymbol{\theta}_j} \\ &= \left[ \boldsymbol{\theta}_1 \cdot \mathbf{n}(\mathbf{y}) e^{ik\boldsymbol{\theta}_1 \cdot \mathbf{y}}, \boldsymbol{\theta}_2 \cdot \mathbf{n}(\mathbf{y}) e^{ik\boldsymbol{\theta}_2 \cdot \mathbf{y}}, \dots, \boldsymbol{\theta}_N \cdot \mathbf{n}(\mathbf{y}) e^{ik\boldsymbol{\theta}_N \cdot \mathbf{y}} \right]^T \end{aligned} \quad (7)$$

and where  $\mathbb{Q}_N(\hat{\mathbf{x}}, \mathbf{y})$  is the corresponding density vector

$$\mathbb{Q}_N(\hat{\mathbf{x}}, \mathbf{y}) = \left[ \psi(\mathbf{y}, \boldsymbol{\theta}_1), \psi(\mathbf{y}, \boldsymbol{\theta}_2), \dots, \psi(\mathbf{y}, \boldsymbol{\theta}_N) \right]^T. \quad (8)$$

Formula (6) is the factorization of the MSR matrix that separates the known incoming plane-wave information from the unknown information similar to the Dirichlet boundary condition case. The range of  $\mathbb{K}$  is determined by the span of the  $\mathbb{P}_N(\hat{\mathbf{x}}, \mathbf{y})$  corresponding to  $\Gamma$ . Hence, on the basis of the result in [12], by applying a set of remaining singular vectors of  $\mathbb{K}$ , a signal subspace can be defined.

Let the singular value decomposition of the matrix  $\mathbb{K}$  be

$$\mathbb{K} = \mathbf{U} \mathbf{B} \mathbf{V}^* = \sum_{m=1}^M \sigma_m \mathbf{U}_m \mathbf{V}_m^*,$$

where  $\mathbf{U}_m \in \mathbb{C}^{N \times 1}$  are the left-singular vectors of  $\mathbb{K}$  and  $\sigma_m$  are nonnegative real-valued singular values such that

$$\sigma_1 \geq \sigma_2 \geq \dots \geq \sigma_M > 0 \quad \text{and} \quad \sigma_j = 0 \quad \text{for} \quad j = M+1, M+2, \dots, N.$$

Alternatively,  $\sigma_j$ , for  $j = M+1, M+2, \dots, N$ , could merely be very small, below the noise level of the system represented by  $\mathbb{K}$ . Then, the first  $M$  columns of the matrix  $\mathbf{U}$ ,  $\{\mathbf{U}_1, \mathbf{U}_2, \dots, \mathbf{U}_M\}$ , provide an orthonormal basis for  $\mathbb{K}$  and the rest of the columns,  $\{\mathbf{U}_{M+1}, \mathbf{U}_{M+2}, \dots, \mathbf{U}_N\}$ , provides a basis for the null (or noise) space of  $\mathbb{K}$ . So, one can form the projection onto the null (or noise) subspace: this projection is given explicitly by

$$\mathbf{P}_{\text{noise}} = \mathbb{I} - \sum_{m=1}^M \mathbf{U}_m \mathbf{U}_m^*, \quad (9)$$

where  $\mathbb{I}$  denotes  $N \times N$  identity matrix.

On the basis of  $\mathbb{P}_N(\hat{\mathbf{x}}, \mathbf{y})$  in (7), for any  $\mathbf{z} \in \mathbb{R}^2$  and  $\mathbf{c}_n \in \mathbb{R}^2 \setminus \{\mathbf{0}\}$ , define  $\mathbf{f}(\mathbf{z}) \in \mathbb{C}^{N \times 1}$  as

$$\mathbf{f}(\mathbf{z}) = \left[ (\mathbf{c}_1 \cdot \boldsymbol{\theta}_1) e^{ik\boldsymbol{\theta}_1 \cdot \mathbf{z}}, (\mathbf{c}_2 \cdot \boldsymbol{\theta}_2) e^{ik\boldsymbol{\theta}_2 \cdot \mathbf{z}}, \dots, (\mathbf{c}_N \cdot \boldsymbol{\theta}_N) e^{ik\boldsymbol{\theta}_N \cdot \mathbf{z}} \right]^T. \quad (10)$$

Then, there exists  $N_0 \in \mathbb{N}$  such that for any  $N \geq N_0$ , the following statement holds [21]:

$$\mathbf{f}(\mathbf{z}) \in \text{Range}(\mathbb{K}) \quad \text{if and only if} \quad \mathbf{z} \in \{\mathbf{y}_1, \mathbf{y}_2, \dots, \mathbf{y}_M\}.$$

This means that if a point  $\mathbf{z}$  satisfies  $\mathbf{z} \in \{\mathbf{y}_1, \mathbf{y}_2, \dots, \mathbf{y}_M\}$  then  $|\mathbf{P}_{\text{noise}}(\mathbf{f}(\mathbf{z}))| = 0$ . Thus, an image of  $\mathbf{y}_m \in \Gamma$ ,  $m = 1, 2, \dots, M$ , can be obtained from computing

$$\mathbb{W}(\mathbf{z}) = \frac{1}{|\mathbf{P}_{\text{noise}}(\mathbf{f}(\mathbf{z}))|}. \quad (11)$$

The resulting plot of  $\mathbb{W}(\mathbf{z})$  is expected to exhibit peaks of large (theoretically,  $+\infty$ ) magnitude at the  $\mathbf{y}_m \in \Gamma$ .

### 3. Mathematical structure and intrinsic properties of imaging functional

On the basis of the results in [14], the selection of  $\mathbf{c}_n$  is a strong prerequisite. The selection depends on the shape of the supporting curve  $\Gamma$ . Roughly speaking,  $\mathbf{c}_n$  must be of the form  $\mathbf{n}(\mathbf{x}_m)$  for  $m = 1, 2, \dots, M$ . Unfortunately, we have no *a priori* information of shape of  $\Gamma$ . Due to this reason, in [12, 14], a large number of directions are applied in order to find an optimal vector  $\mathbf{c}_n$  but this process requires large computational costs. Hence, motivated from recent work [13, 22], we assume that  $\mathbf{c}_n$  satisfies  $\mathbf{c}_n \cdot \boldsymbol{\theta}_n = 1$  for all  $n$ . Correspondingly, instead of (10), we apply

$$\mathbf{f}(\mathbf{z}) = \frac{1}{\sqrt{N}} \left[ e^{ik\boldsymbol{\theta}_1 \cdot \mathbf{z}}, e^{ik\boldsymbol{\theta}_2 \cdot \mathbf{z}}, \dots, e^{ik\boldsymbol{\theta}_N \cdot \mathbf{z}} \right]^T, \quad (12)$$

and explore some properties of MUSIC-type imaging algorithm.

#### 3.1. Relationship with Bessel function of first order

Before starting, we recall a useful relationship, which plays a key roll of our identification.

**Lemma 3.1.** Assume that  $\{\boldsymbol{\theta}_n : n = 1, 2, \dots, N\}$  spans  $\mathbb{S}^1$ . Then, for sufficiently large  $N$ ,  $\boldsymbol{\xi} \in \mathbb{S}^1$ , and  $\mathbf{x} \in \mathbb{R}^2$ .

$$\frac{1}{N} \sum_{n=1}^N (\boldsymbol{\theta}_n \cdot \boldsymbol{\xi}) e^{ik\boldsymbol{\theta}_n \cdot \mathbf{x}} = \frac{1}{2\pi} \int_{\mathbb{S}^1} (\boldsymbol{\theta} \cdot \boldsymbol{\xi}) e^{ik\boldsymbol{\theta} \cdot \mathbf{x}} dS(\boldsymbol{\theta}) = i \left( \frac{\mathbf{x}}{|\mathbf{x}|} \cdot \boldsymbol{\xi} \right) J_1(k|\mathbf{x}|),$$

where  $J_\nu$  denotes the Bessel function of integer order  $\nu$  of the first kind.

Now, we state the main result.

**Theorem 3.2.** Let  $N > M$ . Then, for sufficiently large  $N$  and  $k$ , (11) can be written as follows:

$$\mathbb{W}(\mathbf{z}) = \left( 1 - 2 \sum_{m=1}^M \left( \frac{\mathbf{z} - \mathbf{y}_m}{|\mathbf{z} - \mathbf{y}_m|} \cdot \mathbf{n}(\mathbf{y}_m) \right)^2 J_1(k|\mathbf{z} - \mathbf{y}_m|)^2 \right)^{-1/2}. \quad (13)$$

*Proof.* Let us consider the polar-coordinate representation: for  $\boldsymbol{\theta}, \boldsymbol{\xi} \in \mathbb{S}^1$ ,  $\boldsymbol{\theta} = [\cos \theta, \sin \theta]^T$ , and  $\boldsymbol{\xi} = [\cos \psi, \sin \psi]^T$ . Since

$$\sum_{n=1}^N (\boldsymbol{\theta}_n \cdot \boldsymbol{\xi})^2 \approx \frac{N}{2\pi} \int_{\mathbb{S}^1} (\boldsymbol{\theta} \cdot \boldsymbol{\xi})^2 d\boldsymbol{\theta} = \frac{N}{2\pi} \int_0^{2\pi} \cos^2(\phi - \psi) d\phi = \frac{N}{2}, \quad (14)$$

the left singular vectors are of the form (see [8])

$$\mathbf{U}_m \approx \sqrt{\frac{2}{N}} \left[ (\boldsymbol{\theta}_1 \cdot \mathbf{n}(\mathbf{y}_m)) e^{ik\boldsymbol{\theta}_1 \cdot \mathbf{y}_m}, (\boldsymbol{\theta}_2 \cdot \mathbf{n}(\mathbf{y}_m)) e^{ik\boldsymbol{\theta}_2 \cdot \mathbf{y}_m}, \dots, (\boldsymbol{\theta}_N \cdot \mathbf{n}(\mathbf{y}_m)) e^{ik\boldsymbol{\theta}_N \cdot \mathbf{y}_m} \right]^T.$$

Since, we select  $\mathbf{f}(\mathbf{z})$  as (12),  $\mathbf{P}_{\text{noise}}$  can be written as

$$\begin{aligned} \mathbf{P}_{\text{noise}}(\mathbf{f}(\mathbf{z})) &= \left( \mathbb{I}_N - \sum_{m=1}^M \mathbf{U}_m \bar{\mathbf{U}}_m^T \right) \mathbf{f}(\mathbf{z}) \\ &\approx \frac{1}{\sqrt{N}} \begin{bmatrix} e^{ik\boldsymbol{\theta}_1 \cdot \mathbf{z}} \\ e^{ik\boldsymbol{\theta}_2 \cdot \mathbf{z}} \\ \vdots \\ e^{ik\boldsymbol{\theta}_N \cdot \mathbf{z}} \end{bmatrix} - \frac{2}{N\sqrt{N}} \sum_{m=1}^M \begin{bmatrix} (\boldsymbol{\theta}_1 \cdot \mathbf{n}(\mathbf{y}_m)) e^{ik\boldsymbol{\theta}_1 \cdot \mathbf{y}_m} \sum_{n=1}^N (\boldsymbol{\theta}_n \cdot \mathbf{n}(\mathbf{y}_m)) e^{ik\boldsymbol{\theta}_n \cdot (\mathbf{z} - \mathbf{y}_m)} \\ (\boldsymbol{\theta}_2 \cdot \mathbf{n}(\mathbf{y}_m)) e^{ik\boldsymbol{\theta}_2 \cdot \mathbf{y}_m} \sum_{n=1}^N (\boldsymbol{\theta}_n \cdot \mathbf{n}(\mathbf{y}_m)) e^{ik\boldsymbol{\theta}_n \cdot (\mathbf{z} - \mathbf{y}_m)} \\ \vdots \\ (\boldsymbol{\theta}_N \cdot \mathbf{n}(\mathbf{y}_m)) e^{ik\boldsymbol{\theta}_N \cdot \mathbf{y}_m} \sum_{n=1}^N (\boldsymbol{\theta}_n \cdot \mathbf{n}(\mathbf{y}_m)) e^{ik\boldsymbol{\theta}_n \cdot (\mathbf{z} - \mathbf{y}_m)} \end{bmatrix} \\ &= \frac{1}{\sqrt{N}} \begin{bmatrix} e^{ik\boldsymbol{\theta}_1 \cdot \mathbf{z}} - 2i \sum_{m=1}^M (\boldsymbol{\theta}_1 \cdot \mathbf{n}(\mathbf{y}_m)) \left( \frac{\mathbf{z} - \mathbf{y}_m}{|\mathbf{z} - \mathbf{y}_m|} \cdot \mathbf{n}(\mathbf{y}_m) \right) e^{ik\boldsymbol{\theta}_1 \cdot \mathbf{y}_m} J_1(k|\mathbf{z} - \mathbf{y}_m|) \\ e^{ik\boldsymbol{\theta}_2 \cdot \mathbf{z}} - 2i \sum_{m=1}^M (\boldsymbol{\theta}_2 \cdot \mathbf{n}(\mathbf{y}_m)) \left( \frac{\mathbf{z} - \mathbf{y}_m}{|\mathbf{z} - \mathbf{y}_m|} \cdot \mathbf{n}(\mathbf{y}_m) \right) e^{ik\boldsymbol{\theta}_2 \cdot \mathbf{y}_m} J_1(k|\mathbf{z} - \mathbf{y}_m|) \\ \vdots \\ e^{ik\boldsymbol{\theta}_N \cdot \mathbf{z}} - 2i \sum_{m=1}^M (\boldsymbol{\theta}_N \cdot \mathbf{n}(\mathbf{y}_m)) \left( \frac{\mathbf{z} - \mathbf{y}_m}{|\mathbf{z} - \mathbf{y}_m|} \cdot \mathbf{n}(\mathbf{y}_m) \right) e^{ik\boldsymbol{\theta}_N \cdot \mathbf{y}_m} J_1(k|\mathbf{z} - \mathbf{y}_m|) \end{bmatrix}. \end{aligned}$$

Hence, we can obtain

$$|\mathbf{P}_{\text{noise}}(\mathbf{f}(\mathbf{z}))| = \left( \frac{1}{N} \sum_{n=1}^N \left( 1 + \Psi_1 - \bar{\Psi}_1 + \Psi_2 \bar{\Psi}_2 \right) \right)^{1/2},$$

where

$$\begin{aligned}\Psi_1 &= 2i \sum_{m=1}^M (\boldsymbol{\theta}_n \cdot \mathbf{n}(\mathbf{y}_m)) \left( \frac{\mathbf{z} - \mathbf{y}_m}{|\mathbf{z} - \mathbf{y}_m|} \cdot \mathbf{n}(\mathbf{y}_m) \right) e^{ik\boldsymbol{\theta}_n \cdot (\mathbf{z} - \mathbf{y}_m)} J_1(k|\mathbf{z} - \mathbf{y}_m|) \\ \Psi_2 &= 2 \sum_{m=1}^M (\boldsymbol{\theta}_n \cdot \mathbf{n}(\mathbf{y}_m)) \left( \frac{\mathbf{z} - \mathbf{y}_m}{|\mathbf{z} - \mathbf{y}_m|} \cdot \mathbf{n}(\mathbf{y}_m) \right) e^{ik\boldsymbol{\theta}_n \cdot \mathbf{y}_m} J_1(k|\mathbf{z} - \mathbf{y}_m|).\end{aligned}$$

Since

$$\begin{aligned}\sum_{n=1}^N \Psi_1 &= 2i \sum_{n=1}^N \sum_{m=1}^M (\boldsymbol{\theta}_n \cdot \mathbf{n}(\mathbf{y}_m)) \left( \frac{\mathbf{z} - \mathbf{y}_m}{|\mathbf{z} - \mathbf{y}_m|} \cdot \mathbf{n}(\mathbf{y}_m) \right) e^{ik\boldsymbol{\theta}_n \cdot (\mathbf{z} - \mathbf{y}_m)} J_1(k|\mathbf{z} - \mathbf{y}_m|) \\ &= 2i \sum_{m=1}^M \left( \frac{\mathbf{z} - \mathbf{y}_m}{|\mathbf{z} - \mathbf{y}_m|} \cdot \mathbf{n}(\mathbf{y}_m) \right) \sum_{n=1}^N \left( (\boldsymbol{\theta}_n \cdot \mathbf{n}(\mathbf{y}_m)) e^{ik\boldsymbol{\theta}_n \cdot (\mathbf{z} - \mathbf{y}_m)} \right) J_1(k|\mathbf{z} - \mathbf{y}_m|) \\ &= -2N \sum_{m=1}^M \left( \frac{\mathbf{z} - \mathbf{y}_m}{|\mathbf{z} - \mathbf{y}_m|} \cdot \mathbf{n}(\mathbf{y}_m) \right)^2 J_1(k|\mathbf{z} - \mathbf{y}_m|)^2,\end{aligned}$$

we can obtain

$$\frac{1}{N} \sum_{n=1}^N (\Psi_1 - \bar{\Psi}_1) = -4 \sum_{m=1}^M \left( \frac{\mathbf{z} - \mathbf{y}_m}{|\mathbf{z} - \mathbf{y}_m|} \cdot \mathbf{n}(\mathbf{y}_m) \right)^2 J_1(k|\mathbf{z} - \mathbf{y}_m|)^2. \quad (15)$$

Furthermore, we can evaluate

$$\begin{aligned}\sum_{n=1}^N \Psi_2 \bar{\Psi}_2 &= 4 \sum_{n=1}^N \left( \sum_{m=1}^M (\boldsymbol{\theta}_n \cdot \mathbf{n}(\mathbf{y}_m)) \left( \frac{\mathbf{z} - \mathbf{y}_m}{|\mathbf{z} - \mathbf{y}_m|} \cdot \mathbf{n}(\mathbf{y}_m) \right) e^{ik\boldsymbol{\theta}_n \cdot \mathbf{y}_m} J_1(k|\mathbf{z} - \mathbf{y}_m|) \right) \\ &\quad \times \left( \sum_{m'=1}^M (\boldsymbol{\theta}_n \cdot \mathbf{n}(\mathbf{y}_{m'})) \left( \frac{\mathbf{z} - \mathbf{y}_{m'}}{|\mathbf{z} - \mathbf{y}_{m'}|} \cdot \mathbf{n}(\mathbf{y}_{m'}) \right) e^{-ik\boldsymbol{\theta}_n \cdot \mathbf{y}_{m'}} J_1(k|\mathbf{z} - \mathbf{y}_{m'}|) \right) \\ &= 4 \sum_{m=1}^M \sum_{n=1}^N \left( (\boldsymbol{\theta}_n \cdot \mathbf{n}(\mathbf{y}_m))^2 \left( \frac{\mathbf{z} - \mathbf{y}_m}{|\mathbf{z} - \mathbf{y}_m|} \cdot \mathbf{n}(\mathbf{y}_m) \right)^2 J_1(k|\mathbf{z} - \mathbf{y}_m|)^2 \right) \\ &= 4N \sum_{m=1}^M \left( \frac{1}{N} \sum_{n=1}^N (\boldsymbol{\theta}_n \cdot \mathbf{n}(\mathbf{y}_m))^2 \right) \left( \frac{\mathbf{z} - \mathbf{y}_m}{|\mathbf{z} - \mathbf{y}_m|} \cdot \mathbf{n}(\mathbf{y}_m) \right)^2 J_1(k|\mathbf{z} - \mathbf{y}_m|)^2 \\ &= 2N \sum_{m=1}^M \left( \frac{\mathbf{z} - \mathbf{y}_m}{|\mathbf{z} - \mathbf{y}_m|} \cdot \mathbf{n}(\mathbf{y}_m) \right)^2 J_1(k|\mathbf{z} - \mathbf{y}_m|)^2.\end{aligned}$$

Hence, we can conclude that

$$\frac{1}{N} \sum_{n=1}^N \Psi_2 \bar{\Psi}_2 = 2 \sum_{m=1}^M \left( \frac{\mathbf{z} - \mathbf{y}_m}{|\mathbf{z} - \mathbf{y}_m|} \cdot \mathbf{n}(\mathbf{y}_m) \right)^2 J_1(k|\mathbf{z} - \mathbf{y}_m|)^2. \quad (16)$$

Therefore, by (15) and (16), we can obtain

$$|\mathbf{P}_{\text{noise}}(\mathbf{f}(\mathbf{z}))| = \left\{ 1 - 2 \sum_{m=1}^M \left( \frac{\mathbf{z} - \mathbf{y}_m}{|\mathbf{z} - \mathbf{y}_m|} \cdot \mathbf{n}(\mathbf{y}_m) \right)^2 J_1(k|\mathbf{z} - \mathbf{y}_m|)^2 \right\}^{1/2}.$$

With this, we can derive (13). This completes the proof.  $\square$

### 3.2. Intrinsic properties of imaging functional

Based on the structure (13), we can observe following some intrinsic properties of MUSIC-type imaging functional.

- (P1). Total number of incident and observation directions  $N$  must be sufficiently large. Furthermore, based on the relationship between imaging functional and Bessel function, imaging result is highly depending on the applied wavenumber. So,  $k$  must be large enough. These assumptions in Theorem 3.2 are very strong *a priori* conditions, refer to the simulation results in Section 4.
- (P2). Since  $J_1(1.8412)' \approx 0$ ,  $J_1$  has its maximum value 0.5819 at  $x \approx 1.8412$ . Therefore,

$$2 \left( \frac{\mathbf{z} - \mathbf{y}_m}{|\mathbf{z} - \mathbf{y}_m|} \cdot \mathbf{n}(\mathbf{y}_m) \right)^2 J_1(k|\mathbf{z} - \mathbf{y}_m|)^2 \leq 2(0.5819)^2 = 0.6772 \neq 1.$$

This means that there is no blow-up of  $\mathbb{W}(\mathbf{z})$ .

- (P3). On the basis of the shape of  $J_1(x)^2$  (see Figure 1), instead of true shape, two curves will appear along the normal direction in the neighborhood of  $\Gamma$ . Related discussion can be found in [12, 13, 22] and numerical results in Section 4. Note that following asymptotic form holds

$$J_1(k|\mathbf{z} - \mathbf{y}_m|)^2 \approx \left( \frac{k|\mathbf{z} - \mathbf{y}_m|}{2} \right)^2 \quad \text{for } 0 < k|\mathbf{z} - \mathbf{y}_m| \ll \sqrt{2},$$

it is expected that true shape of  $\Gamma$  can be imaged via the map of  $\mathbb{W}(\mathbf{z})$  when  $k \rightarrow +\infty$ . However, this is an ideal assumption.

- (P4). Following recent work [11], it is expected that vectors  $\mathbf{c}_n$ ,  $n = 1, 2, \dots, N$ , in (10) can be estimated. Then, the structure of  $\mathbb{W}(\mathbf{z})$  becomes (see [13] for instance)

$$\mathbb{W}(\mathbf{z}) \approx \left( 1 - \sum_{m=1}^M J_0(k|\mathbf{z} - \mathbf{y}_m|)^2 \right)^{-1/2}$$

correspondingly, almost true shape of  $\Gamma$  can be obtained. Related results are exhibited in [14].

- (P5). Based on recent works [22, 8, 23], applying multi-frequency improves the imaging performance. However, in the imaging of sound-hard arc, application of multi-frequency will reduce the artifacts but true shape of crack cannot be retrieved.



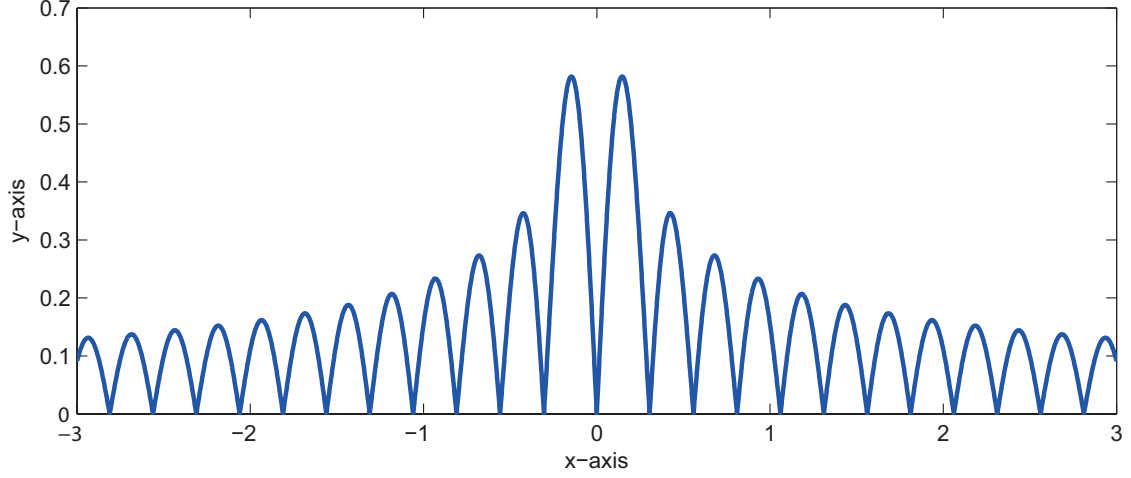


Figure 1: 1-D plot of  $|J_1(kx)|$  for  $k = 2\pi/0.5$ .

#### 4. Simulation results and discussions

In this section, some results of numerical simulations with noisy data are exhibited for supporting our result in Theorem 3.2. Throughout this section, two curves  $\Gamma_j$  are chosen to describe the sound-hard arc such that

$$\begin{aligned}\Gamma_1 &= \{[s - 0.2, -0.5s^2 + 0.4] : -0.5 \leq s \leq 0.5\}, \\ \Gamma_2 &= \{[s + 0.2, s^3 + s^2 - 0.4] : -0.5 \leq s \leq 0.5\}.\end{aligned}$$

Total number of incident and observation directions is set to  $N = 32$  and incident vectors  $\boldsymbol{\theta}_l$  are selected as

$$\boldsymbol{\theta}_l = - \left[ \cos \frac{2\pi(l-1)}{N-1}, \sin \frac{2\pi(l-1)}{N-1} \right]^T.$$

It is worth mentioning that, since the reliable and efficient solution of the direct scattering problem indicated previously is very important, elements  $u_\infty(\theta_j, \theta_l)$  for  $j, l = 1, 2, \dots, N$  of the  $\mathbb{K}$  are generated by solving second-kind Fredholm integral equation along the crack, refer to [24, Section 3]. After obtaining the dataset, 20-dB white Gaussian random noise is added to the unperturbed data via the MATLAB subroutine `awgn`. In order to perform the singular value decomposition of  $\mathbb{K}$ , MATLAB subroutine `svd` is applied. To obtain the number of nonzero singular values, a 0.01-threshold scheme (select the first  $M$ -values  $\sigma_m$  that  $\sigma_m/\sigma_1 \geq 0.01$ ) is adopted. A more detailed discussion of threshold can be found in [14, 15] (see [12] for the volumetric-extended target case).

First, let us consider the imaging of  $\Gamma_1$ . Figure 2 exhibits the maps of  $\mathbb{W}(\mathbf{z})$  for  $\lambda = \pi$ , 0.8, 0.4, and 0.2. It is easy to observe that two ghost replicas with large magnitude in the neighborhood of  $\Gamma_1$  so that observation (P3) holds. The shape of  $\Gamma_1$  cannot be identified via the map of  $\mathbb{W}(\mathbf{z})$  if applied value of  $k$  is small. In contrast, if  $k$  is sufficiently large, one can identify two curves. This supports the observation (P1). Furthermore, if  $k$  becomes large,

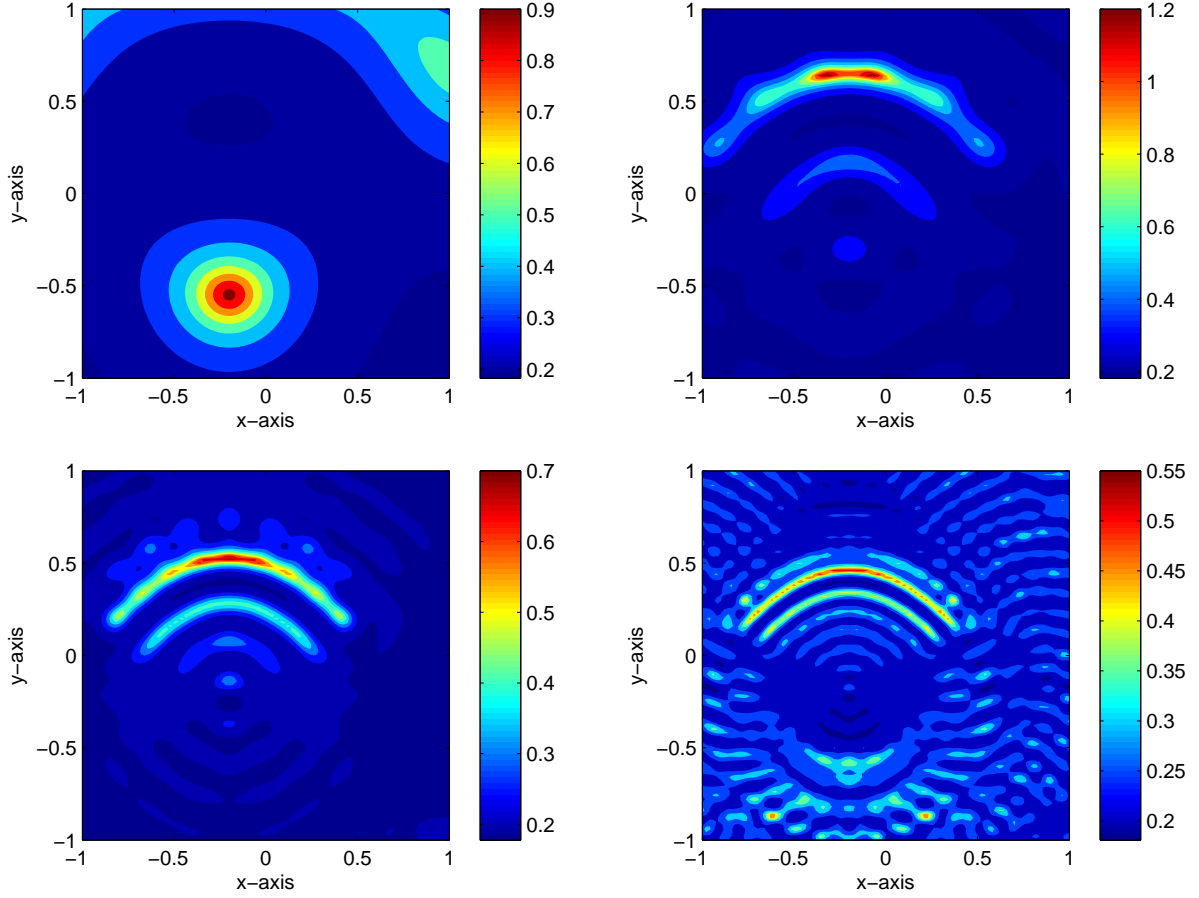


Figure 2: Maps of  $\mathbb{W}(\mathbf{z})$  for  $\lambda = \pi$  (top, left),  $\lambda = 0.8$  (top, right),  $\lambda = 0.4$  (bottom, left), and  $\lambda = 0.2$  (bottom, right) when the crack is  $\Gamma_1$ .

identified shape is close to the true shape of  $\Gamma_1$ . Hence, although it is an ideal assumption, if  $k = +\infty$ , true shape of  $\Gamma_1$  can be recognized via the map of  $\mathbb{W}(\mathbf{z})$ , refer to (P3). Notice that for selected values of  $k$ , maximum value of  $\mathbb{W}(\mathbf{z})$  is not so large enough. Hence, there is no blow-up of  $\mathbb{W}(\mathbf{z})$  and this supports observation (P2).

Figure 3 shows the maps of  $\mathbb{W}(\mathbf{z})$  for  $\lambda = \pi, 0.8, 0.4$ , and  $0.2$  when the crack is  $\Gamma_2$ . Similar to the previous result, this result supports the analysis derived in Theorem 3.2.

It is well-known that the mathematical setting and the numerical analysis could be extended straightforwardly to multiple cracks. For the final example, we consider the imaging of two cracks  $\Gamma_1 \cup \Gamma_2$  with  $N = 48$  total directions, refer to Figure 4. Similar to the previous results, we can recognize two curves along  $\Gamma_1$  and  $\Gamma_2$  when sufficiently large  $k = 2\pi/0.2$  is applied. But, it is very hard to identify the existence of cracks with small  $k$ .

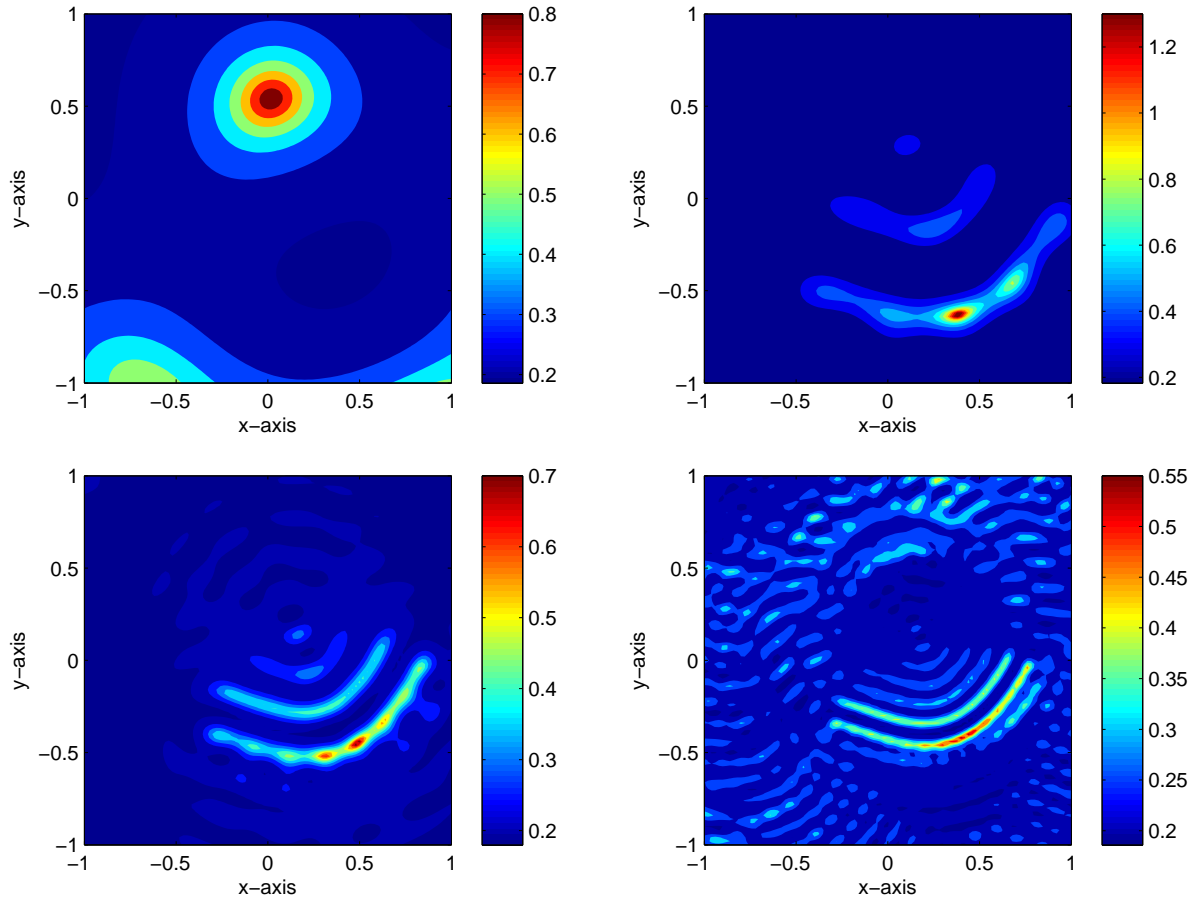


Figure 3: Same as Figure 2 except the crack is  $\Gamma_2$ .

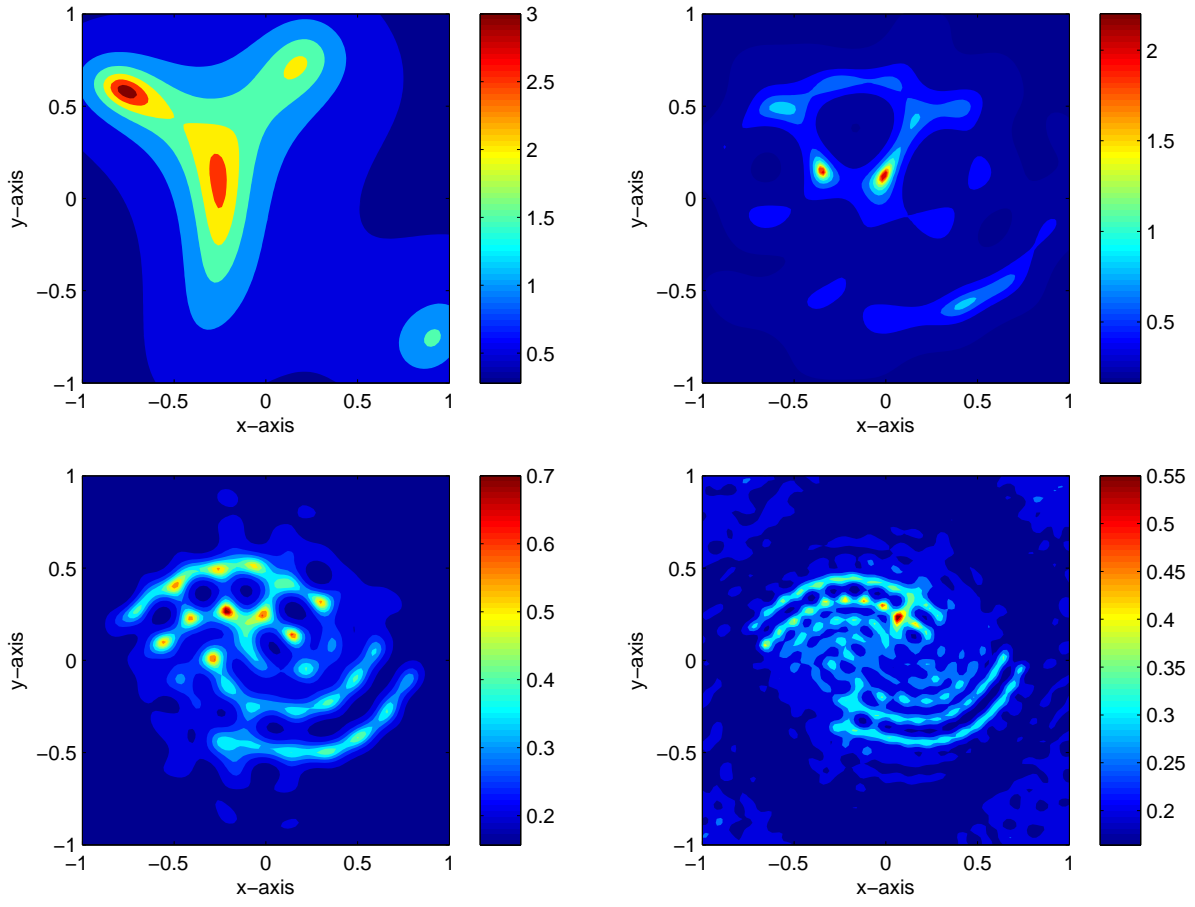


Figure 4: Same as Figure 2 except the crack is  $\Gamma_2$ .

## 5. Conclusion

We considered MUSIC-type algorithm for imaging of sound-hard arc. Based on the relationship between MUSIC-type imaging function and Bessel function of order 1 of the first kind, we examined intrinsic properties and limitation of MUSIC.

Although we considered MUSIC-type imaging in full-view inverse scattering problem, based on our contributions [7, 18], MUSIC is also applicable to limited-view inverse problem with appropriate condition of the range of incident and observation direction. Discovering certain properties of MUSIC in limited-view problem will be an interesting research topic.

## References

- [1] L. Mönch, On the numerical solution of the direct scattering problem for an open sound-hard arc, *J. Comput. Appl. Math.* 17 (1996) 343–356.
- [2] L. Mönch, On the inverse acoustic scattering problem by an open arc: the sound-hard case, *Inverse Problems* 13 (1997) 1379–1392.
- [3] C. J. S. Alves, P. Serranho, On the identification of the flatness of a sound-hard acoustic crack, *Math. Comput. Simulat.* 66 (2004) 337–353.
- [4] R. Kress, P. Serranho, A hybrid method for sound-hard obstacle reconstruction, *J. Comput. Appl. Math.* 204 (2007) 418–427.
- [5] K.-M. Lee, Inverse scattering from a sound-hard crack via two-step method, *Abstr. Appl. Anal.* 2012 (2012) 810676.
- [6] K.-M. Lee, Inverse scattering via nonlinear integral equations for a Neumann crack, *Inverse Problems* 22 (2006) 1989–2000.
- [7] C. Y. Ahn, K. Jeon, W.-K. Park, Analysis of MUSIC-type imaging functional for single, thin electromagnetic inhomogeneity in limited-view inverse scattering problem, *J. Comput. Phys.* 291 (2015) 198–217.
- [8] H. Ammari, J. Garnier, H. Kang, W.-K. Park, K. Sølna, Imaging schemes for perfectly conducting cracks, *SIAM J. Appl. Math.* 71 (2011) 68–91.
- [9] H. Ammari, E. Iakovleva, D. Lesselier, A MUSIC algorithm for locating small inclusions buried in a half-space from the scattering amplitude at a fixed frequency, *Multiscale Model. Simul.* 3 (2005) 597–628.
- [10] H. Ammari, H. Kang, H. Lee, W.-K. Park, Asymptotic imaging of perfectly conducting cracks, *SIAM J. Sci. Comput.* 32 (2010) 894–922.
- [11] X. Chen, Y. Zhong, MUSIC electromagnetic imaging with enhanced resolution for small inclusions, *Inverse Problems* 25 (2009) 015008.
- [12] S. Hou, K. Sølna, H. Zhao, A direct imaging algorithm for extended targets, *Inverse Problems* 22 (2006) 1151–1178.
- [13] W.-K. Park, Asymptotic properties of MUSIC-type imaging in two-dimensional inverse scattering from thin electromagnetic inclusions, *SIAM J. Appl. Math.* 75 (2015) 209–228.
- [14] W.-K. Park, D. Lesselier, Electromagnetic MUSIC-type imaging of perfectly conducting, arc-like cracks at single frequency, *J. Comput. Phys.* 228 (2009) 8093–8111.
- [15] W.-K. Park, D. Lesselier, MUSIC-type imaging of a thin penetrable inclusion from its far-field multi-static response matrix, *Inverse Problems* 25 (2009) 075002.
- [16] B. Scholz, Towards virtual electrical breast biopsy: space frequency MUSIC for trans-admittance data, *IEEE Trans. Med. Imag.* 21 (2002) 588–595.
- [17] Y. Zhong, X. Chen, MUSIC imaging and electromagnetic inverse scattering of multiple-scattering small anisotropic spheres, *IEEE Trans. Antennas Propag.* 55 (2007) 3542–3549.
- [18] Y.-D. Joh, Y. M. Kwon, W.-K. Park, MUSIC-type imaging of perfectly conducting cracks in limited-view inverse scattering problems, *Appl. Math. Comput.* 240 (2014) 273–280.

- [19] Y.-D. Joh, W.-K. Park, Structural behavior of the MUSIC-type algorithm for imaging perfectly conducting cracks, *Prog. Electromagn. Res.* 138 (2013) 211–226.
- [20] H. Ammari, E. Bonnetier, Y. Capdeboscq, Enhanced resolution in structured media, *SIAM J. Appl. Math.* 70 (2009) 1428–1452.
- [21] H. Ammari, H. Kang, Reconstruction of Small Inhomogeneities from Boundary Measurements, vol. 1846 of *Lecture Notes in Mathematics*, Springer-Verlag, Berlin, 2004.
- [22] W.-K. Park, Multi-frequency subspace migration for imaging of perfectly conducting, arc-like cracks in full- and limited-view inverse scattering problems, *J. Comput. Phys.* 283 (2015) 52–80.
- [23] W.-K. Park, Analysis of a multi-frequency electromagnetic imaging functional for thin, crack-like electromagnetic inclusions, *Appl. Numer. Math.* 77 (2014) 31–42.
- [24] Z. T. Nazarchuk, *Singular Integral Equations in Diffraction Theory*, Mathematics and Applications Series, Karpenko Physicomechanical Institute, Ukrainian Academy of Sciences, Lviv, 1994.